Project work

Knut Emil Ringstad

Moving Immersed Boundary Method for Compressible Flow

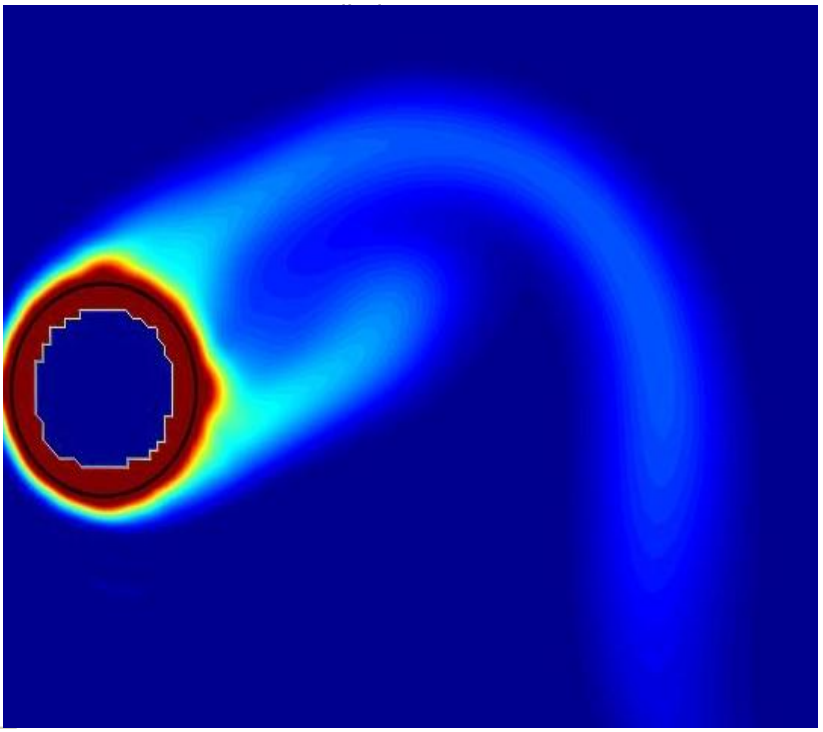

NTNU
Norwegian University of Science and Technology
Faculty of Engineering
Department of Energy and Process Engineering

NTNU – Trondheim
Norwegian University of Science and Technology

Norwegian University of Science and Technology

Faculty of Engineering
Department of Energy and Process Engineering

EPT-P-2017-93

NTNU

PROJECT WORK

for

student Knut Emil Ringstad

Autumn 2017

Moving Immersed Boundary Method for Compressible Flow
Bevegelig nedsenket grense metode for kompressibel strømning

Background and objective

Opposed to body-fitted grid methods, the surface of a body intersects the grid lines in an immersed boundary method (IBM). For the surface boundary of the body is immersed in a Cartesian grid. The solid wall boundary conditions can be imposed by assigning values to ghost points inside the solid body adjacent to the immersed boundary such that the ghost point values reflect the presence of the body surface. In IBM, the difficult task of generating body-fitted grids is replaced by flagging fluid, ghost and solid points. For moving bodies, this flagging in IBM has to be done dynamically. We investigate a moving IBM for compressible viscous flow starting from an existing IBM code for stationary bodies.

The goal of the project is to implement, verify and validate the IBM for moving bodies in 2D compressible viscous flow.

The following tasks are to be considered:

1. to get a basic physical understanding of viscous compressible flow, its mathematical description and its numerical solution by immersed boundary methods (IBMs),
2. to extend an IBM for stationary bodies to moving bodies for the 2D compressible Navier-Stokes equations,
3. to implement that moving IBM into an existing IBM 2D compressible Navier-Stokes code for stationary bodies,
4. to verify and validate the new moving IBM for 2D compressible viscous flow,
5. to write a scientific report.

-- " --

The project work comprises 15 ECTS credits.

Address
N-7034 Trondheim
Norway

Location
K. Hejes vei 1b

Tel. +47 73 59 38 60
Fax +47 73 59 35 80
Org. no. NO 974 767 880

The work shall be edited as a scientific report, including a table of contents, a summary in Norwegian, conclusion, an index of literature etc. When writing the report, the candidate must emphasise a clearly arranged and well-written text. To facilitate the reading of the report, it is important that references for corresponding text, tables and figures are clearly stated both places.
By the evaluation of the work the following will be greatly emphasised: The results should be thoroughly treated, presented in clearly arranged tables and/or graphics and discussed in detail.

The candidate is responsible for keeping contact with the subject teacher and teaching supervisors.

Risk assessment of the candidate's work shall be carried out according to the department's procedures. The risk assessment must be documented and included as part of the final report. Events related to the candidate's work adversely affecting the health, safety or security, must be documented and included as part of the final report. If the documentation on risk assessment represents a large number of pages, the full version is to be submitted electronically to the supervisor and an excerpt is included in the report.

According to "Utfyllende regler til studieforskriften for teknologistudiet/sivilingeniørstudiet ved NTNU" § 20, the Department of Energy and Process Engineering reserves all rights to use the results and data for lectures, research and future publications.

The report shall be submitted to the department via Blackboard.

Submission deadline: 21 December 2017.

☐ Work to be done in lab (Water power lab, Fluids engineering lab, Thermal engineering lab)
☐ Field work

Department for Energy and Process Engineering, *17 August 2017*

Bernhard Müller
Supervisor

Abstract

In this report a ghost-point immersed boundary method for the compressible Navier-Stokes equations using a higher order summation by parts operator is described. The implementation of isothermal boundary conditions at steady and moving immersed boundaries is described and validated for stationary cylinders in laminar cross flow. The method shows good capability to describe the isothermal boundary conditions for stationary cylinders. A potential improvement of the boundary layer approximation for the pressure boundary condition is described. A convergence study showed second order convergence for flow around a stationary cylinder at Re=100. Simulations with oscillating cylinder indicate that a finer resolution is required for the description of heat transfer on moving bodies.

The figure on the title page is given in figure (5.7) in the report.

Acknowledgments

I would like to thank my supervisor Bernhard Müller for his great guidance and motivation during this project work. I would also like to extend my gratitude to Ehsan Khalili for all the help and explanations offered.

Table of contents

List of Tables

List of Figures

List of symbols and abbreviations

Symbols

ρ	=	Mass density
μ	=	Dynamic viscosity
τ	=	Viscous stress tensor
γ	=	Ratio of specific heats
κ	=	Heat conduction coefficient
ϕ	=	Generic variable
t	=	Physical time
x, y	=	Cartesian coordinates in physical domain
ξ,η	=	Transformed coordinates in computational domain
E	=	Specific total energy
H	=	Total entalpy
p	=	Pressure
Sc	=	Sutherland constant
T	=	Temperature
U	=	Vector of conservative variables
$\vec{n}$	=	normal vector
$\vec{\sigma}$	=	tangential vector

Abbreviations

GP	=	Ghost point
IP	=	Image point
BI	=	Body intercept
CFD	=	Computational fluid dynamics
IBM	=	Immersed boundary method
OSAS	=	Obstructive sleep apnea syndrome
SBP	=	Summation by parts

Chapter 1

Introduction

Computational fluid dynamics (CFD) for biomedical applications has received growing attention. It is becoming a key tool for understanding and designing for flows in the human body. CFD can affordably and non-invasively be applied to patient specific models and even evaluate proposed surgical procedures [13]. Its application shows promise for the modeling of flow in the nasal airways [13] and cardiovascular system [5]. However it is a complicated and difficult task owing to the complex geometry and modelling task. For example the biomedical properties of tissue of the human upper airways, cf. figure (1.1), have to be modelled and the experimental data for validation are difficult to obtain. Modern imaging techniques makes it possible, but not simple, to obtain the required geometries, but these are at quite low resolution and patient-specific. Still, CFD has shown promise for the modelling of the airflow in the airways, and new advances allow modelling of the interaction between the fluid and the biological structures [22].

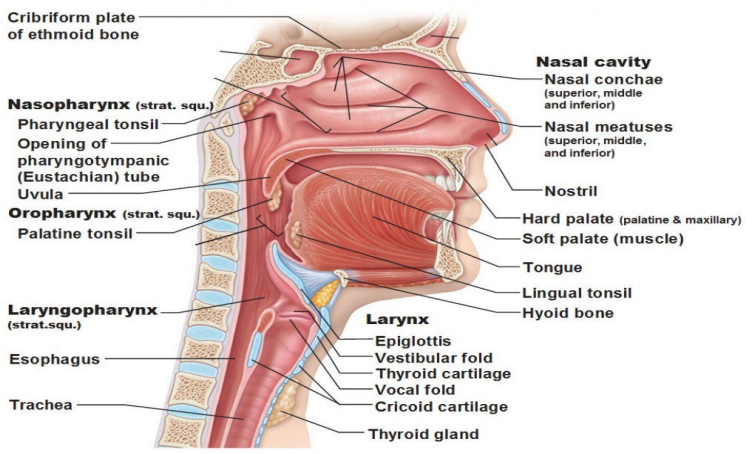

Figure 1.1: Illustration of the human upper airways [23]

This report is extending the work by Khalili et al. [12] for the research project ”Modeling of obstructive sleep apnea by fluid-structure inter-action in the upper airways” funded by the Research Council of Norway. The goal is to extend the immersed boundary method for moving bodies.
The report is structured as follows. In chapter 2 a review of the current literature on the topics of the immersed boundary method, higher order summation by parts method and heat transfer for oscillating bodies is given. In chapter 3 some background theory for compressible flow and heat transfer is presented. In chapter 4 the numerical model is described. The immersed boundary method is presented including the implementation of isothermal boundary conditions at the immersed boundaries. An alternative boundary condition for pressure is presented. In chapter 5 the results of the simulations are presented and the method is verified and validated against available experimental and numerical data. The conclusions are given in chapter 6. Suggestions for further work are presented in chapter 7.

Chapter 2

Literature review

2.1 Immersed boundary method

The immersed boundary method (IBM) was first used by Peskin [26] as a method to investigate blood flow in the heart. The premise of the method is to define the unknown variables on a equidistant Cartesian grid and impose the boundary conditions indirectly on the flow variables. This boundary condition imposition was done with a forcing term added to the discretization of the equations.
Fadlun et al. [6] later imposed the boundary conditions by setting flow variables at grid points, called ghost points, adjacent to the boundary such that when averaged over the flow field adjacent to the boundary each boundary condition was satisfied at the boundary. That IBM was named the ghost cell IBM (GCIBM).
A very dense grid is required for proper resolution of the boundary layer. A grid adaptation for GCIBM methods has been done by Wang and Wu [34].
Hylla and Thiele [9] implemented a fluid-structure-interaction model with a ghost-cell IBM using an incompressible flow solver and a linear finite element method for simulation of flow around elastic cylinders.
Luo et al. [16] investigated GCIBM for different boundary conditions using a compressible solver and showed second order accuracy for Robin, Neumann and Dirichlet boundary conditions.
Turbulence models have been implemented into GCIBM solvers using large eddy simulation (LES) for turbulent compressible [21] and incompressible flows [33].
The GCIBM has also recently been used by Sun and Shao-Fan [31] for improvements on terrain models for weather forecasting.
The implementation of the GCIBM was improved by Manish [17] to achieve better mass conservation and computational overhead for an incompressible solver. Heat transfer for the high order GCIBM method was investigated for a sphere by Xia et al. [36], and multi-particle inter-phase heat transfer in [35] using the cut-cell method in 3D.

2.2 Higher order summation by parts method

The Summation by Parts (SBP) operator is a finite difference method to approximate the first derivative such that the discrete analogue of integration by parts is satisfied [8]. That discretization ensures that the energy of a hyperbolic system is bounded by the initial condition. The idea is to get a stable method by making a discretization scheme corresponding to the terms of the integration by parts form of the hyperbolic equation. This finite difference method was introduced by Kreiss and Scherer [14][15]. Higher order SBP operators with diagonal discrete norm matrices were devised by Strand [30] with order $2s$ in the interior and order s near the boundaries, $s = 1, 2, 3, 4$. To keep the method stable during time integration a weakly imposed boundary condition was suggested by Carpenter et al. [3]. This is done by a boundary term called the "simultaneous approximation term" (SAT), this term is applying the boundary condition by "dragging" the computed boundary value towards the prescribed boundary value by a differential equation. Later SBP operators of the second space derivative for parabolic problems were devised by Mattsson and Nordström [18].

2.3 Heat transfer for transversely oscillating cylinders

Heat transfer from steady and moving bodies is an vital design aspect in many engineering disciplines, such as mechanical-, chemical- and HVAC-engineering. Heat transfer from steady cylinders in cross flow is one of the most studied cases of heat transfer and has become an important benchmark when validating CFD methods. Park and Gharib [25] and Pottebaum and Gharib [28] studied heat transfer from oscillating cylinders for different transitional and turbulent Reynolds numbers. In these articles also oscillation frequencies and amplitudes were investigated. From what has been found, little experimental research has been done for heat transfer over an oscillating cylinder for low Reynolds numbers. The results of this report will be compared to Cheng and Chen [4] for Re=200.

Chapter 3

Background theory

3.1 Compressible gas dynamics

The full 2D compressible Navier-Stokes (NS) equations are considered. These are a system of transport equations: the continuity equation for the density of the fluid (3.1), the momentum equation for the two components of the momentum density (3.2) and the energy equation for the total energy (3.3). This gives four equations for six variables, including the pressure and temperature. The system is closed by the equations of state (3.4-3.5). The compressible Navier-Stokes without external forces can be written with the Einstein summation convention:

$$\frac{\partial \rho}{\partial t} + \frac{\partial}{\partial x_j}\left[\rho u_j\right] = 0, \tag{3.1}$$

$$\frac{\partial}{\partial t}\left(\rho u_i\right) + \frac{\partial}{\partial x_j}\left[\rho u_i u_j + p\delta_{ij} - \tau_{ij}\right] = 0, \quad i = 1, 2, \tag{3.2}$$

$$\frac{\partial}{\partial t}\left(\rho E\right) + \frac{\partial}{\partial x_j}\left[\rho u_j E + u_j p + q_j - u_i \tau_{ij}\right] = 0, \tag{3.3}$$

where ρ, u_1, u_2, p, E are the mass density, x- and y-velocity components, pressure and specific total energy respectively.

The equations of state for perfect gas are used:

$$p = \rho R T, \tag{3.4}$$

$$e = c_v T, \tag{3.5}$$

where $e = E - \frac{1}{2}|u_1^2 + u_2^2|$ is the specific internal energy, R, c_v, T are the gas constant of the fluid, specific heat capacity at constant volume and temperature respectively. These equations are solved in dimensionless, perturbation form, discussed in section (4.1).

The viscous stress tensor for compressible flows is defined as:

$$\tau_{ij} = \mu(\frac{\partial u_i}{\partial x_j} + \frac{\partial u_j}{\partial x_i}) - \frac{2\mu}{3}\frac{\partial u_k}{\partial x_k}\delta_{ij}, \tag{3.6}$$

where μ is the viscosity of the fluid. The viscosity is determined by the Sutherland law $\frac{\mu}{\mu_0} = (\frac{T}{T_0})^{1.5}[(1 + Sc)/(\frac{T}{T_0} + Sc)]$. Where S_c is the dimensionless Sutherland constant, $S_c = \frac{110}{301.75}$.

The heat flux q_j is defined as:

$$q_j = -\kappa\frac{\partial T}{\partial x_j}, \tag{3.7}$$

where κ is the thermal conductivity of the fluid.

The pressure can be related to the conservative variables by

$$p = (\gamma - 1)(\rho E - \frac{1}{2}|u_1^2 + u_2^2|) \tag{3.8}$$

where γ is the ratio of specific heats $\gamma = c_p/c_v$ = 1.4 for air.

3.2 Heat transfer

Heat transfer is described in fluid dynamics by the physical transport of energy (3.3). For a heated body in a flow the heat is transported from the surface by three mechanisms, conduction, radiation and convection. Convection is the transport of heat by relative motion of the surrounding fluid, while conduction is the transport of heat by random motion on the molecular scale. Radiation describes heat transfer by electromagnetic waves, these effects are assumed negligible and not included in the energy equation (3.3). Convection and conduction effects appear in the heat transport equation of compressible flow as; $\frac{\partial(\rho E+p)}{\partial x_j}$ and $\frac{\partial q_j}{\partial x_j}$ respectively.

A ratio for the relative magnitude of total heat transfer over the conductive heat transfer can be defined by a dimensionless number called the Nusselt number:

$$Nu_L = \frac{hL}{\kappa}, \tag{3.9}$$

where h is the heat transfer coefficient of the flow, L is the characteristic length, κ is the thermal conductivity of the fluid.

The heat transfer coefficient is defined as the ratio of the total heat transfer by convection and conduction over the temperature difference of the fluid and the solid surface.

$$h = \frac{q}{\Delta T}, \tag{3.10}$$

3.3 Laminar flow around a circular cylinder

The laminar flow around a circular cylinder is a classical fluid mechanics problem and is often used as a benchmark problem for CFD-solvers. Laminar flow around a circular cylinder is characterized by three regimes [37];
- Very low Reynolds number flow, $Re < 5$, where the flow does not separate from the cylinder, also referred to as creeping flow.
-Intermediate Reynolds number flows, $5 < Re < 50$, where the flow is characterized by a steady symmetric wake behind the cylinder.
-High Reynolds number flows, $50 < Re < 200$, characterized by an unstable wake region causing oscillating shear layers to shed vortices with alternating rotation.

The transition from laminar to turbulent flow takes place over a range of Reynolds numbers, the onset happens in the wake behind the cylinder at Reynolds numbers above approximately 180 [37]. The Reynolds number is defined as:

$$Re_D = \frac{UD}{\nu}, \tag{3.11}$$

where U is the undisturbed flow velocity, D is the cylinder diameter and ν is the dynamic fluid viscosity.

3.4 Flow around an oscillating cylinder

Transverse oscillations of a cylinder in a cross flow is a complex flow problem due to the interaction between the fluid and the oscillating body. Forced oscillation as a sinusoidal function at different frequencies and amplitudes are of special interest due to the interaction of the oscillation- and the natural vortex shedding-frequency. One such phenomenon is the synchronization of the vortex shedding frequency with the forced oscillation frequency, referred to as "lock-in". The dimensionless oscillating frequency $St = \frac{fD}{u_0}$, is called the Strouhalt number.

Chapter 4

Model description

4.1 Compressible Navier Stokes in conservative form

The compressible Navier Stokes equations (3.1-3.3) are solved in conservative form for the vector of the conserved unknown variables $\vec{U}$:

$$\vec{U} = \begin{pmatrix} \rho \\ \rho u \\ \rho v \\ \rho E \end{pmatrix} \tag{4.1}$$

The variables are defined in dimensionless, perturbation form. The variables are solved for the perturbation of the variables from the stagnation values, $\vec{U_0} = (\rho_0, 0, 0, (\rho E)_0)^T$. This is further described in [11]. The variables $\vec{U}$ are then non-dimensionalized by $\rho_0, \rho_0 c_0, \rho_0 c_0, \rho_0 c_0^2$, respectively. In this form the compressible Navier Stokes equations can be written as:

$$\vec{U}_t + \vec{F}_x^c + \vec{G}_y^c = \vec{F}_x^v + \vec{G}_y^v \tag{4.2}$$

where F and G are the flux-vectors in the x- and y-directions respectively, the subscripts indicate differentiation by that variable, the superscript c indicates the convective flux vectors and v the viscous flux vectors, defined as:

$$\vec{F}^c = \begin{pmatrix} \rho u \\ (\rho u)u + p \\ (\rho u)v \\ ((\rho H)_0 + \rho H)u \end{pmatrix} \qquad \vec{G}^c = \begin{pmatrix} \rho v \\ (\rho v)u \\ (\rho v)v + p \\ ((\rho H)_0 + \rho H)v \end{pmatrix} \tag{4.3}$$

$$\vec{F}^v = \begin{pmatrix} 0 \\ \tau_{xx} \\ \tau_{xy} \\ \tau_{xx}u + \tau_{xy}v + \kappa T_x \end{pmatrix} \qquad \vec{G}^v = \begin{pmatrix} 0 \\ \tau_{yx} \\ \tau_{yy} \\ \tau_{yx}u + \tau_{yy}v + \kappa T_y \end{pmatrix} \tag{4.4}$$

where $(\rho H)_0 = (\rho E)_0 + p_0$ is the stagnation total enthalpy per unit volume.

Constant Prandtl numbers $Pr = \frac{\mu c_p}{\kappa}$ were considered and the ratio of specific heat for air $\gamma = 1.4$ was used. The τ_{ij} terms are the components of the viscous stress tensor of equation (3.6).

4.2 Coordinate transformation

The equations are solved on a 2D Cartesian grid under a coordinate transformation. The grid transformation is done to improve grid quality the near the cylinder as seen in figure (4.1). The transformed coordinates (ξ, η) are found by the coordinate transformation $\xi = \xi(x, y)$, $\eta = \eta(x, y)$. The coordinate transformation is described in [11]. The transformed 2D compressible Navier-Stokes equations are then written as:

$$\vec{\hat{U}}_t + \vec{\hat{F}}_\xi + \vec{\hat{G}}_\eta = 0 \tag{4.5}$$

where $\hat{U} = J^{-1}U$,$\hat{F} = J^{-1}(\xi_x(F^c - F^v) + \xi_y(G^c - G^v))$ and $\hat{G} = J^{-1}(\eta_x(F^c - F^v) + \eta_y(G^c - G^v))$. The Jacobian determinant of the transformation is $J^{-1} = x_\xi y_\eta - x_\eta y_\xi$ and metric terms are:

$$\begin{aligned} J^{-1}\xi_x &= y_\eta, & J^{-1}\xi_y &= -x_\eta \\ J^{-1}\eta_x &= -y_\xi, & J^{-1}\eta_y &= x_\xi \end{aligned}$$

For simplicity the ξ and η derivatives will be referred to as the normal x- and y derivatives in this report. This corresponds to the trivial transformation: $\frac{\partial \xi}{\partial x} = 1$, $\frac{\partial \eta}{\partial y} = 1$, $\frac{\partial \xi}{\partial y} = 0$, $\frac{\partial \xi}{\partial y} = 0$.

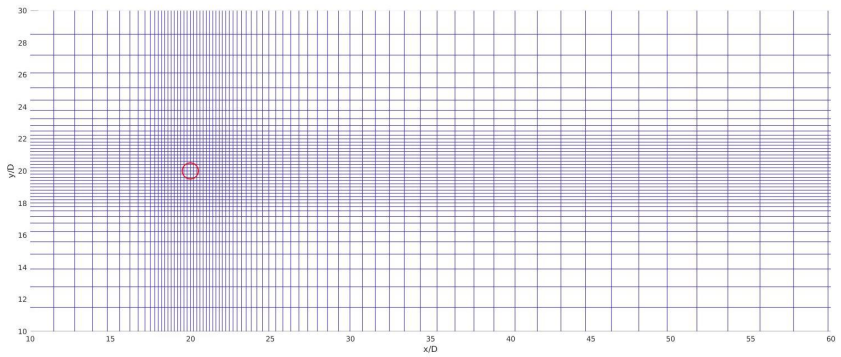

Figure 4.1: Cartesian grid near the cylinder for [x=18D 22D]x[y=18D 22D], and stretched grid away from the cylinder. Every 5 lines is plotted

4.3 Numerical method

The method uses the standard central 6th order accurate finite difference stencil for the discretization of the first derivative in space in the interior, i.e. the $\vec{F}_x^c, \vec{G}_y^c, \vec{F}_x^v, \vec{G}_y^v$ -terms in equation (4.2). The viscous flux vector terms, $\vec{F}^v, \vec{G}^v$, in equation (4.4) need additional discretizations for their internal derivative terms; τ_{ij} and $(\kappa T)_x, (\kappa T)_y$, this is done by applying the first derivative approximation again. Near the boundaries of the domain and near the immersed boundary a 3rd order finite difference is applied, the method as a whole gives a global 4th order of accuracy in space[30][20]. The spacial discretization is based on the Summation By Parts operator method, a method that improves stability and will keep the energy of the system bounded by the initial conditions if proper boundary conditions are applied, see section 2.2. The in- and outflow boundary conditions are applied by injection of the Navier-Stokes characteristic BC [27][11].

For time discretization the classical explicit 4-stage Runge-Kutta method is used giving a 4th order accurate solution in time. How the moving immersed boundaries are treated by the time discretization is discussed in section 4.6.

4.4 Ghost point immersed boundary method

The immersed boundary method is a method for imposing different boundary conditions at a defined boundary in a grid system. The two most common ways of imposing the required boundary conditions are by forcing terms or ghost points. In this report the ghost-point approach is discussed. The most conventional and common way to handle boundary conditions, such as a wall, is to make the grid conform to the body and thereby imposing the boundary condition at the grid points fitted to the boundary. This is referred to as a body-fitted grid. The mesh generation of highly complex or moving geometries is a computationally heavy and complicated task for any body fitted grid. The immersed boundary method avoids this problem by keeping a simple, usually Cartesian, grid and treating the boundary conditions at internal boundaries indirectly. This boundary can with much lower computational cost be moved by recalculating where and how to impose the new boundary conditions. In the ghost-point version of the IBM the indirect imposition of these boundary conditions is done by wisely setting the values of flow variables on the solid side of the boundary. These points are lying inside the solid (see figure 4.2). However the ghost points are treated by the discretized equations as fluid points, and so they affect the flow variables at the fluid points outside the boundary. Due to their effect on the fluid points without themselves being ”real” fluid points they are referred to as ghost-points. Points inside the solid which do not appear in the discretized equations are considered solid points. An illustration of this general case is in figure (4.2). How the values at these ghost points are chosen is described in section 4.5. The idea of the method is to set the flow variables at the ghost points in such a way that when averaged over the flow variables adjacent to the boundary the boundary condition is respected at the boundary intersection (BI) point. For a Dirichlet boundary condition this means that the average value at the imposed boundary is equal to the boundary value.

To impose the boundary condition well a large number of grid points is required near the boundary. If the geometry of the boundary has a sharp turn, such as near the trailing

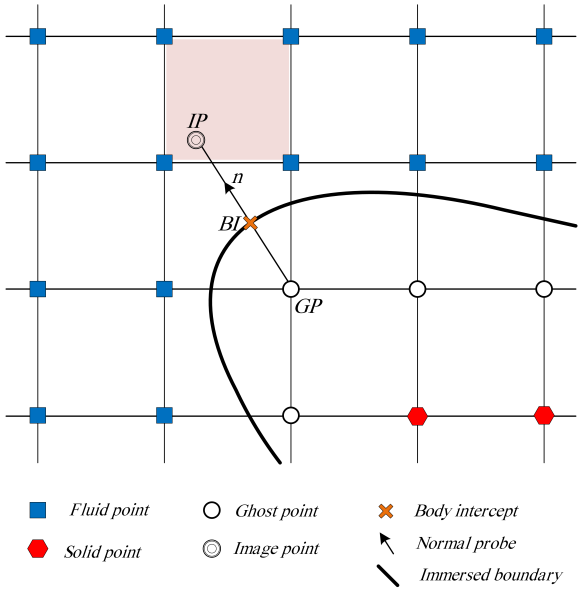

Figure 4.2: Illustration of the ghost-, image- and boundary intersect-points [11]

edge of a wing profile, the body may contain fewer ghost points than is needed for the higher order discretization. The method would then require special treatment. This is however not required for this geometry and not covered by this IBM.

4.5 Ghost point imposed boundary conditions

The physical boundary conditions imposed at solid boundaries are discussed here. For compressible flow four boundary conditions are needed to close the system. The boundary conditions used in the work by [11] are the no slip-condition for the momentum-equations, the adiabatic wall for the energy equation and the boundary layer approximation Neumann condition for the for the pressure.

$$\vec{u} = \vec{U}_{wall}, \tag{4.6}$$

$$\frac{\partial T}{\partial n} = 0, \tag{4.7}$$

$$\frac{\partial p}{\partial n} = 0 \tag{4.8}$$

where $\vec{U}_{wall}$ is the prescribed velocity of the wall and n denotes the wall normal direction.

By the perfect gas law; $\rho = \frac{RT}{P}$ (3.4), the boundary condition for the density can be found, closing the system and enforcing the adiabatic wall condition eqn. (4.7) by:

$$\frac{d\rho}{dn} = \frac{d(\frac{RT}{p})}{dn} = 0. \tag{4.9}$$

However this simplification is not possible when a Dirichlet isothermal boundary condition is imposed instead of equation (4.7). The isothermal boundary condition is further discussed in section 4.7.

4.5.1 Implementation of ghost point boundaries

To implement the physical boundary conditions at the boundary of the body the ghost points are given values such that the correct condition is applied at the immersed boundary. For a generic variable ϕ a Dirichlet condition would be imposed by setting the ghost point value ϕ_{gp} such that the average of the ghost point value and the value at its corresponding image point (ip) imposes the condition $\phi_{bi} = \phi_{boundary}$, where bi is the boundary intersection point, that is to say equation (4.10) holds. The image point is the reflection point of the ghost point mirrored in the wall normal direction with respect to the body intercept, see figure (4.2). An illustration is given in figure (4.3) of how multiple layers the different ghost points are treated. For a cylinder finding the mirror point is straightforward as all points normal to the immersed boundary are lying along the radial direction. To calculate the value at the image point bilinear interpolation is used as described in section 4.7.2.

$$\frac{\phi_{gp} + \phi_{ip}}{2} = \phi_{bi} \tag{4.10}$$

A Neumann condition, $\frac{\partial \phi}{\partial n} = \zeta$, can be similarly imposed by setting the ghost point such that the change of ϕ across the boundary is the given condition ζ. Thus the ghost point value ϕ_{gp} should be set such that the difference between the ghost point value and the image point value over the distance between them imposes the boundary condition. This is described by:

$$\frac{\phi_{ip} - \phi_{gp}}{\Delta l} = \zeta. \tag{4.11}$$

4.6 Moving immersed boundaries

This immersed boundary method is well suited for moving geometries compared to body fitted grids. To update the geometry for a new time step the position of the new boundary is evaluated. From this boundary new ghost points and fluid points can be found. The boundary conditions are applied at the new boundary, now the no-slip condition for the velocity can be calculated by the movement of the boundary. The no-slip condition (4.6) now becomes:

$$\vec{u}_{bi} = \frac{\partial \vec{x}_S}{\partial t}, \tag{4.12}$$

where $\vec{x}_S$ is the position of the solid boundary. For transverse oscillations in the y-direction this becomes:

$$v_{bi} = \frac{\partial y_S}{\partial t},$$

where y_S can be described as a sinusoidal function: $y_S(t) = Asin(\omega t + \psi) + y_0$.

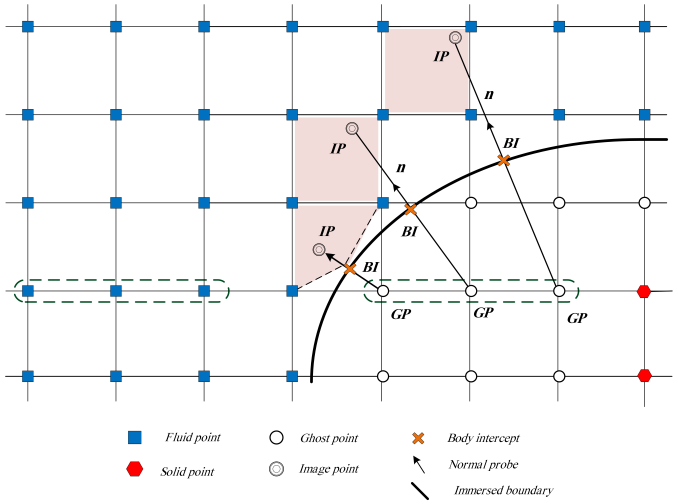

Figure 4.3: Illustration of the ghost-, image- and boundary intersect-points, [11]

The moving boundary is implemented in [11] by relocating the immersed boundary. For this simple movement this corresponds to moving the center of the cylinder according to the sinusoidal function. The ghost points are then found and calculated as to impose the boundary condition on the new moved boundary. This relocation is done before all four stages of the Runge-Kutta method are calculated. One issue that is encountered with the moving boundaries is the problem of freshly emerged fluid points. This occurs when a solid point, inside the body, is changed to a fluid point, outside the body, by the movement of the immersed boundary in one time step. This causes a temporal discontinuity as a solid point would hold no information about previous time steps. This is solved in this IBM [11] by a bi-linear interpolation of the variables surrounding the freshly emerged point. The problem is however limited as the CFL condition bounds the movement of the immersed boundary. This implies that any new fluid points has been a ghost point, as long as the ghost-cell layer is at least one deep [12].

The temporal discretization of the immersed boundary movement is based on the classical explicit Runge-Kutta 4-stage method. The intermediate movement of the boundary between the Runge-Kutta stages is not taken into account. This suggests that the method should degenerate to lower than fourth order accuracy. This is complicated to investigate and is discussed in section 5.2.1. A pseudo-code of the algorithm from time level n to n + 1 for the calculation of moving immersed boundaries, as presented in Khalili et al. [12], is included for clarity (adapted for this report):

Move boundary to time level n + 1.
Set the classical RungeKutta stage level $l = 1$.

1: Determine u_{gp}, v_{gp}, T_{gp} and p_{gp} using eqn. 4.11 and 4.10 at three layers of ghost point based on solution $\vec{U}^{(l)}$, the choices of boundary conditions for flow variables are discussed in section 4.5.1. From eqn. 4.16; ρ_{gp} can be found.

2: Compute approximations of the viscous fluxes F^v and G^v at all fluid and ghost points using the sixth order SBP operator on each line in ξ and η directions, respectively.

3: Compute the residual $R(\vec{U}^{(l)})$ based on the approximations of the derivatives F_ξ and G_η at all fluid points determined by using the sixth order SBP operator on each line in ξ and η directions, respectively, but the standard sixth order difference operator near the immersed boundary.

4: Determine $\vec{U}^{(l+1)}$ using the classical RungeKutta method.

5: Apply the Navier Stokes characteristic boundary condition at inlet and outlet and apply the necessary boundary conditions at the bottom and top boundaries to determine $\vec{U}^{(l)}$ at those boundaries.

6: Set $l := l + 1$.

7: **if** $l < 5$ then

8: **goto** 1

9: **else**

10: Compute $U^{(n+1)}$ at all fluid points.

11: Apply sixth order filter operators in ξ and η directions at all fluid points.

12: **end if**

Here l corresponds to the stage of the classical explicit Runge-Kutta method, n corresponds to the time level. The mentioned filter in step 11 is further explained in [11].

4.7 Implementation of the isothermal boundary condition

To study heat transfer for isothermal moving walls the isothermal boundary condition on moving bodies is considered. The Neumann condition eqn. (4.7) for adiabatic walls is then exchanged by the isothermal Dirichlet condition:

$$T_{bi} = T_{wall} \tag{4.13}$$

The boundary layer approximation for the pressure will be used. An alternative boundary condition will be discussed in section 4.7.1.

By the boundary conditions (4.13) and (4.6), ghost point values u_{gp}, v_{gp}, T_{gp} can be found from equation (4.10), where the Dirichlet boundary condition ϕ_{bi} corresponds to the isothermal eqn. (4.13) and no slip eqn. (4.6) respectively. By the boundary condition (4.8) a ghost point value for p_{gp} can be found by equation (4.11), where the Neumann boundary condition ζ is given by the boundary layer approximation eqn. (4.8).

The boundary layer approximation, equation (4.8), and the perfect gas law can be applied to obtain:

$$p_{gp} = p_{ip}, \tag{4.14}$$

$$(\rho RT)_{gp} = p_{ip}, \tag{4.15}$$

$$\rho_{gp} = \frac{p_{ip}}{RT_{gp}}. \tag{4.16}$$

These ghost point values give the value for the total energy at the ghost points in 2D by the pressure relation (3.8):

$$(\rho E)_{gp} = \frac{p_{gp}}{\gamma - 1} + \frac{(\rho u)^2_{gp} + (\rho v)^2_{gp}}{2\rho_{gp}} \tag{4.17}$$

4.7.1 The momentum balance approximation for pressure

Steady wall

The boundary layer approximation, $\frac{\partial p}{\partial n} = 0$, as a boundary condition is less appropriate for low Reynolds numbers and near separation points [29]. An alternative boundary condition for the pressure is considered here. An improved pressure boundary condition for the wall can be found by the momentum equation (3.2). Let $\vec{n}$ denote the unit vector normal to the solid boundary First considering a no-slip wall at rest, $u_{iwall} = 0, i = 1, 2$, equation (3.2) reduces to:

$$\frac{\partial}{\partial x_j} \left[p\delta_{ij} - \tau_{ji} \right] |_{wall} = 0 \quad i = 1, 2. \tag{4.18}$$

For a wall the pressure derivative condition in x_i-direction yields:

$$\frac{\partial p}{\partial x_i}_{wall} = \frac{\partial \tau_{ji}}{\partial x_j}_{wall} = \frac{\partial}{\partial x_j} \left(\mu(\frac{\partial u_j}{\partial x_i} + \frac{\partial u_i}{\partial x_j}) - \frac{2\mu}{3} \frac{\partial u_k}{\partial x_k} \delta_{ij} \right). \tag{4.19}$$

For a wall normal in the n-direction, $n = n_i x_i$, in 2D this yields:

$$\begin{aligned} \frac{\partial p}{\partial n}_{wall} = \mathrm{n}_i \frac{\partial p}{\partial x_i}_{wall} = \mathrm{n}_y \left[\frac{\partial}{\partial x} \left(\mu(\frac{\partial u}{\partial y} + \frac{\partial v}{\partial x}) \right) + \frac{\partial}{\partial y} \left(\frac{4\mu}{3} \frac{\partial v}{\partial y} - \frac{2\mu}{3} \frac{\partial u}{\partial x} \right) \right] \\ + \mathrm{n}_x \left[\frac{\partial}{\partial y} \left(\mu(\frac{\partial u}{\partial y} + \frac{\partial v}{\partial x}) \right) + \frac{\partial}{\partial x} \left(\frac{4\mu}{3} \frac{\partial u}{\partial x} - \frac{2\mu}{3} \frac{\partial v}{\partial y} \right) \right], \end{aligned} \tag{4.20}$$

$$\begin{aligned} = \mathrm{n}_y \left(\frac{\partial \mu}{\partial x} \left[\frac{\partial u}{\partial y} + \frac{\partial v}{\partial x} \right] + \frac{\partial \mu}{\partial y} \left[\frac{4}{3} \frac{\partial v}{\partial y} - \frac{2}{3} \frac{\partial u}{\partial x} \right] + \mu(\frac{\partial^2 v}{\partial x^2} + \frac{4}{3} \frac{\partial^2 v}{\partial y^2} + \frac{\partial^2 u}{\partial x \partial y} - \frac{2}{3} \frac{\partial^2 u}{\partial y \partial x}) \right) \\ + \mathrm{n}_x \left(\frac{\partial \mu}{\partial y} \left[\frac{\partial v}{\partial x} + \frac{\partial u}{\partial y} \right] + \frac{\partial \mu}{\partial x} \left[\frac{4}{3} \frac{\partial u}{\partial x} - \frac{2}{3} \frac{\partial v}{\partial y} \right] + \mu(\frac{\partial^2 u}{\partial y^2} + \frac{4}{3} \frac{\partial^2 u}{\partial x^2} + \frac{\partial^2 v}{\partial y \partial x} - \frac{2}{3} \frac{\partial^2 v}{\partial x \partial y}) \right), \end{aligned} \tag{4.21}$$

where u and v are the velocity components in the x- and y-directions respectively.

Assuming constant μ and smoothness of u_i, that is; $\frac{\partial^2 u_i}{\partial x_i \partial x_j} = \frac{\partial^2 u_i}{\partial x_j \partial x_i}$, this yields the equation for the pressure:

$$\frac{\partial p}{\partial n}_{wall} = \mathrm{n}_y \left[\mu(\frac{\partial^2 v}{\partial x^2} + \frac{4}{3} \frac{\partial^2 v}{\partial y^2} + \frac{1}{3} \frac{\partial^2 u}{\partial x \partial y})_{wall} \right] + \mathrm{n}_x \left[\mu(\frac{\partial^2 u}{\partial y^2} + \frac{4}{3} \frac{\partial^2 u}{\partial x^2} + \frac{1}{3} \frac{\partial^2 v}{\partial x \partial y})_{wall} \right] = S. \tag{4.22}$$

The right hand side of this equation will be evaluated by interpolation of nearby fluid points. The assumption of constant viscosity near the wall is reasonable, at least for an isothermal boundary condition. For smooth flow it is reasonable to assume that the velocity components, u and v, are twice continuously differentiable.

The Neumann b.c. (4.22) can be implemented in the IBM by:

$$p_{gp} = p_{ip} - S\Delta l, \tag{4.23}$$

where subscript ip indicate the image point of the ghost point and Δl the distance between them.

Using the equation of state (3.4) for perfect gas, eqn. (4.23) implies:

$$\rho_{gp} = \frac{p_{ip}}{RT_{gp}} - \frac{S\Delta l}{RT_{gp}} \tag{4.24}$$

Where S is the right hand side of equation (4.22). This will yield a better approximation than the boundary layer approximation $\frac{\partial p}{\partial n} = 0$ for the steady wall. However this improvement decreases for smaller Δl, i.e. finer grids. The interpolation can be done by bi-linear interpolation, as described below. Higher order interpolation should be investigated to increase the order near boundaries.

Moving wall

If a moving boundary is considered the no slip condition, $\vec{U}_{wall} = 0$, leading to equation (4.18), does no longer hold, as $\vec{U}|_{wall} \neq 0$. The wall velocity, $\vec{u} = \vec{U}_{wall}$, then appears in the b.c of equation (3.2):

$$\frac{\partial}{\partial t}(\rho u_i) + \frac{\partial}{\partial x_j}\left[\rho u_i u_j + p\delta_{ij} - \tau_{ji}\right] = 0 \quad i = 1, 2 \tag{4.25}$$

For a wall normal in the n-direction in 2D this yields:

$$\frac{\partial p}{\partial n}_{wall} = \left(\frac{\partial \tau_{jn}}{\partial x_j} - \frac{\partial \rho u_n}{\partial t} - \frac{\partial \rho u_n u_j}{\partial x_j}\right)_{wall} \tag{4.26}$$

The form for the viscous term achieved in equation (4.22) is inserted:

$$\begin{aligned}\frac{\partial p}{\partial n}_{wall} = \mathrm{n}_y &\left[\mu\left(\frac{\partial^2 v}{\partial x^2} + \frac{4}{3}\frac{\partial^2 v}{\partial y^2} + \frac{1}{3}\frac{\partial^2 u}{\partial x \partial y}\right) - \left(\frac{\partial \rho u}{\partial t} + \frac{\partial \rho u^2}{x} + \frac{\partial \rho u v}{y}\right)\right]_{wall} \\ +\mathrm{n}_x &\left[\mu\left(\frac{\partial^2 u}{\partial y^2} + \frac{4}{3}\frac{\partial^2 u}{\partial x^2} + \frac{1}{3}\frac{\partial^2 v}{\partial x \partial y}\right) - \left(\frac{\partial \rho v}{\partial t} + \frac{\partial \rho u v}{x} + \frac{\partial \rho v^2}{y}\right)\right]_{wall}\end{aligned} \tag{4.27}$$

The effect of the moving wall term, i.e. the difference of the right hand sides of eqns. (4.27) and (4.21), was investigated by Khalili et al. [12] and was found to be negligible.

4.7.2 Interpolation

Bi-linear interpolation

A variable ϕ, a function of position (x,y) can be defined by bilinear-interpolation of 4 points:

$$\phi(x, y) = C_1 + C_2 x + C_3 y + C_4 xy$$

The coefficients C are found by the solution of the system:

$$VC = \phi$$

where ϕ is the vector of its values at the interpolation points $\phi = (\phi_1, \phi_2, \phi_3, \phi_4)^T$, $\phi_l = \phi(x_l, y_l), l = 1, .., 4$. V is the Vandermonde Matrix:

$$V = \begin{Bmatrix} 1 & x_1 & y_1 & x_1 y_1 \\ 1 & x_2 & y_2 & x_2 y_2 \\ 1 & x_3 & y_3 & x_3 y_3 \\ 1 & x_4 & y_4 & x_4 y_4 \end{Bmatrix}$$

A reformulation described in [7][19] gives a form that only depends on the coordinates of the image point and the four surrounding nodes such that the interpolation point (ip) value can be found:

$$\phi_{ip} = \sum_{j=1}^{4} \alpha_j \phi_j \tag{4.28}$$

If a ghost point lies close to the boundary, the image point might have a number of neighboring ghost points. The interpolation is then corrected to instead take into account the boundary intersection point and the applied boundary condition there [11].

4.8 Calculation of the Nusselt number for validation

The Nusselt number is described and defined in section 3.2. In this case the chosen length scale L is the diameter D of the circular cylinder, i.e. L=D. The average Nusselt number of the circular cylinder is then:

$$Nu_D = \frac{1}{|S|} \int_S \frac{hL}{\kappa} dS = \frac{1}{|S|} \int_S \frac{-\left(\frac{\partial T}{\partial n}\right) D}{T_S - T_{far}} dS \tag{4.29}$$

where T_{far} is the farfield fluid temperature away from the cylinder, S is the 2D surface of the cylinder, $|S|$ is the total length of the curve S. The average Nusselt number is estimated by the trapezoidal rule for summation over the line segments of the cylinder, ΔS:

$$Nu_D = \frac{1}{\sum \Delta S} \sum Nu_{D_{bi}} \Delta S, \tag{4.30}$$

where

$$Nu_{D_{bi}} = \frac{-\left(\frac{\partial T}{\partial n}\right)_{bi} D}{T_{bi} - T_{far}}, \tag{4.31}$$

and T_{bi} is the temperature at the boundary intersection point. The $(\frac{\partial T}{\partial n})_{bi}$ - term in equation (4.31) is calculated by a linear first order differencing approximation:

$$(\frac{\partial T}{\partial n})_{bi} = \frac{T_{ip} - T_{gp}}{\Delta l},$$

where T_{ip}, T_{bi}, T,Δl correspond to the temperature at the image point, the temperature at the boundary intercept point and the distance between these points, respectively.

Chapter 5

Results and discussion

The results of the simulations and discussions are given in this chapter. The description of the simulations can be found in section 5.1. A time step convergence study and a simultaneous grid and time step convergence study is performed to verify the order of the immersed boundary method for steady flow over a circular cylinder, described in section 5.2.1. The method is validated against available experimental and numerical data, respectively, for steady flow over a isothermal circular cylinder in section 5.3.2 and for a transversely oscillating isothermal cylinder in section 5.3.3.

5.1 Description of simulations

The flow cases considered are for flow in a 2D rectangular channel with constant height. The computational domain size is 90Dx40D, where D is the cylinder diameter. The stationary cylinder is located at the position (20D,20.2D) and the oscillating cylinder is initially placed at position (20D,20D). This domain is large enough to reduce boundary- and wave reflection effects [11]. The solutions were calculated on a 441x261 grid, with 115101 grid points in total. The domain is structured by blocks, where the block with the cylinder had the finest grid. In the block containing the cylinder a fine grid spacing of (Δx=Δy=$D/50$) was used. The grid spacing is smoothly stretched to ($\Delta x \approx \Delta y \approx D/2$) near the domain boundaries. The boundary conditions on the domain boundaries are symmetry boundary conditions on the top and bottom walls. The velocity at the inlet is a uniform inflow of $u = U_\infty, v = 0$, the inlet temperature is set to $T = T_0 = 301.75K$. The pressure at the outlet is set to $p = p_0 = p_{atm}$.

The stationary cylinder simulations are initiated with a uniform non-dimensional flow velocity for in the entire domain, $u = 0.03$. The flow will reach a fully developed stage where vortices are shed behind the cylinder with alternating rotation, where the flow is periodically changing with time. Looking at figure (5.1) we see this occurs after non-dimensional time t = 500 for Re=100. As mentioned above the cylinder is placed at position (20,20.2), slightly off center. This small difference made the flow slightly asymmetric which sped up the initial starting of the vortex shedding. The simulations were ran until

non-dimensional time t=650. The oscillating cylinder simulations are initiated similarly. After further inspection it is considered that the flow might not be not be fully developed at this stage, this is further discussed in section 5.2.1.

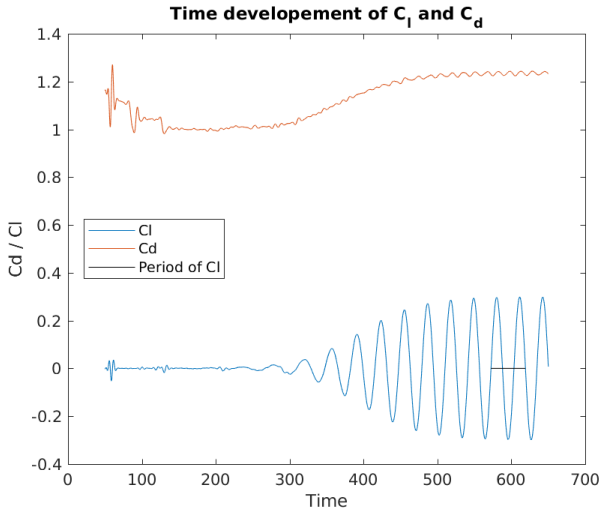

Figure 5.1: Plot of the time development of lift and drag coefficients, steady cylinder Re=100, Ma=0.25

5.1.1 Steady cylinder simulations

Simulations with adiabatic wall were done for the verification of the method. They were done at Re = 100, $Ma_\infty = 0.25$ as to be comparable with numerical and experimental results, [2],[10] and [32], respectively. These are discussed in section 5.2.1 and 5.3.1. Simulations for an isothermal cylinder were done to validate the results for a steady cylinder. The simulations were done at Reynolds numbers 40 and 20, free stream Mach number $Ma_\infty = 0.01$. These were done to validate against the numerical results of Luo et al. [16], Bharti et al. [1] and Pan [24], discussed in section 5.3.2. The dimensionless time step was set to $\Delta t = 10^{-2}$ for these simulations, corresponding to CFL number, C=0.257, and von Neumann number r=0.05. These are below the stability limits for C=1 and $r = \frac{1}{2}$, respectively. The definition of the CFL number and von Neumann number is described in section 5.2.1.

5.1.2 Moving cylinder Simulations

Simulations for a oscillating isothermal circular cylinder were done to validate the method for moving bodies. These were attempted done according to the experimental study by Cheng and Chen [4] at Reynolds number Re=200, free stream Mach number $Ma_\infty = 0.01$. This Reynolds is close to the limit of what the 2D approach can achieve as the flow is close to transitional Reynolds numbers requiring the 3D Navier-Stokes equations to be

solved for direct numerical simulation. The current 2D simulation had to be ran for a long time as to develop any periodic temporal structures, here until non-dimensional time t=2000 was found satisfying. The cylinder was imposed a sinusoidal movement according to $y_S(t) = Asin(\omega t) + y_0$, where y_S is the position of the cylinder center, A is the amplitude of oscillation, ω is the frequency, the cylinder starting position $y_0 = 20D$. The amplitude and frequency was set according to Cheng and Chen [4], $A = 0.628D$. The frequency was intended to be set as the natural Strouhalt frequency, $Sc_0 = 0.16$, however this was wrongly non-dimensionalized as $\omega = Sc_0 Ma_\infty = 0.0016$, instead of $\omega = \frac{Sc_0}{Ma_\infty} = 16$. This made the imposed oscillations frequency far off the natural frequency and validation with experimental data of [4] not possible. The time step was set to $\Delta t = 2 \cdot 10^{-2}$, corresponding to CFL number, C=0.512, and von Neumann number r=0.18. Due to the frequency being set too low there is no concern that the oscillatory movement of the cylinder should violate the CFL-condition.

5.2 Verification

5.2.1 Steady flow over a cylinder

The initial attempt to verify the method using a grid convergence study was done by uniform separate grid spacing- and time step size refinement. As an exact solution is not available for viscous flows around circular cylinders, a solution with refined time step was used as the reference solution for time step size refinement. The reference solution was a simulation with time step $\Delta t = 5 \cdot 10^{-3}$. The error was first assumed of the form: $err(\Delta h, \Delta t) = C_1 \Delta h^p + C_2 \Delta t^q$, where $\Delta h = \Delta x = \Delta y$ is the grid spacing. The methods used are 4th order in both time and space, so the expected order should be $q = p = 4$. However lower order near the boundaries are to be expected owing to the bi-linear interpolation corresponding to second order. The error compared to the reference solution can be written: $err = f(\Delta) - f(\Delta_{reference})$, where Δ is the time step or grid space sizing, the subscript *ref* indicates the reference size, and f is a general function of the solution depending on the grid spacing- and time step size. Halving the time or grid spacing will then reduce the time or spatial error, respectively by $\hat{err} = \frac{err(\frac{\Delta}{2})}{err(\Delta)} \propto (\frac{1}{2})^{(q,p)}$.

Since the tripping of the vortex shedding for the steady flow around a cylinder is dependent on small differences in the simulation, the simulated flows with different refinements will not be comparable until reaching a fully developed stage, as discussed in section 5.1.1. The time step refinement was done by running simulations for three different time step sizes, $\Delta t = 2 \cdot 10^{-2}, 10^{-2}$ and $5 \cdot 10^{-3}$. The lift and drag coefficients are used to compare the convergence rate in time and space at Reynolds number 100. Previously a convergence study of the method has been done by [11] at Reynolds number 40. This convergence study will attempt to verify the method for the unsteady flow at higher Reynolds numbers. The comparison between two grids was done over two periods of the lift coefficient fluctuation. The reference solution used was the solution with a time step refined by a factor 4 compared to the biggest time step. The results of the time step convergence is shown in table 5.1 and figure 5.2. The entries in table 5.1 are the peak to peak values of the lift coefficients, c_l, over one period of fluctuation, the mean of the drag coefficient, $\overline{c}_d$, and the

difference between each solution and the reference solution, err. For a finer time step the simulation result for the lift and drag coefficient appears to deviate further from the results of [2] and [10]. This is further discussed in section 5.3.1.

After the refinement study in time the order of the temporal discretization was estimated to be approximately 1, see figure 5.2 much lower than approximately 4th order expected from the 4-step Runge-Kutta method used. This could be explained by large spatial discretization errors dominating the total error due to the relatively coarse mesh used, i.e. $err(\Delta h) >> err(\Delta t)$.

To investigate this and how the error was reduced by general refinement, a new refinement study was done with refinement in time and space concurrently. This was done by keeping the CFL-number constant at C=0.3 for the different simulations. This implies a linear relation between the time step and the grid spacing. The CFL number is defined in equation (5.1).

$$C = max_{i,j} \left\{ \frac{|u_{i,j}| + c_{i,j}}{\Delta x} + \frac{|v_{i,j}| + c_{i,j}}{\Delta y} \right\} \Delta t \tag{5.1}$$

where C is the CFL number, Δt is the time step, $\Delta x, \Delta y$ is the grid spacing, u, v are the velocity components in x- and y-direction, c is the speed of sound. The indices i,j indicate the point index in the x- and y- direction, respectively. The grid spacing was refined by halving and doubling the grid spacing uniformly in the whole domain. The grid spacing near the cylinder was $\Delta h = \Delta x = \Delta y = D/100$ and $\Delta h = \Delta x = \Delta y = D/25$ for the fine 881x521 grid and coarse 221x131 grid, respectively. The concurrent time refinement was done as above.

Table 5.1: Table of c_l and c_d convergence values for time step refinement for flow over a circular cylinder at Re=100, Ma=0.25 with 441x261 grid, $\Delta h = \Delta x = \Delta y = D/50$, $\Delta t = 10^{-2}$

Grid	$c_{l,\text{peak to peak}}$	$err(c_l)$	$\overline{c}_d$	$err(\overline{c}_d)$
$f(\Delta h, 2\Delta t)$	0.6155	0.0470	1.2423	0.0217
$f(\Delta h, \Delta t)$	0.5964	0.0279	1.2344	0.0138
$f(\Delta h, \frac{\Delta t}{2})^*$	0.5685	-	1.2206	-
Tritton [32](exp), Re=97.3,Ma=0	-	-	1.26	-
Canuto and Taira [2], Re=100,Ma=0.25	0.650	-	1.336	-
Karagiozis et al. [10], Re=100,Ma=0.25	0.638	-	1.378	-

** reference solutions*

The lift and drag coefficients were also here used to investigate the error. The results of the convergence study with a constant CFL number is shown in table 5.2 and figure 5.3. From this it is apparent that the order of the method is approximately $a = 2.2$, where a is the order of accuracy in space and time. The approximately second order accuracy of the method is in good correspondence with the estimated accuracy from [16], where second order spatial accuracy for velocity and temperature near the boundaries was obtained with a similar higher order GCIBM. The results of table 5.2 are discussed in section 5.3.1.

The viscous stability limit for the von Neumann number, r, has been considered. The von Neumann number, r, is defined as:

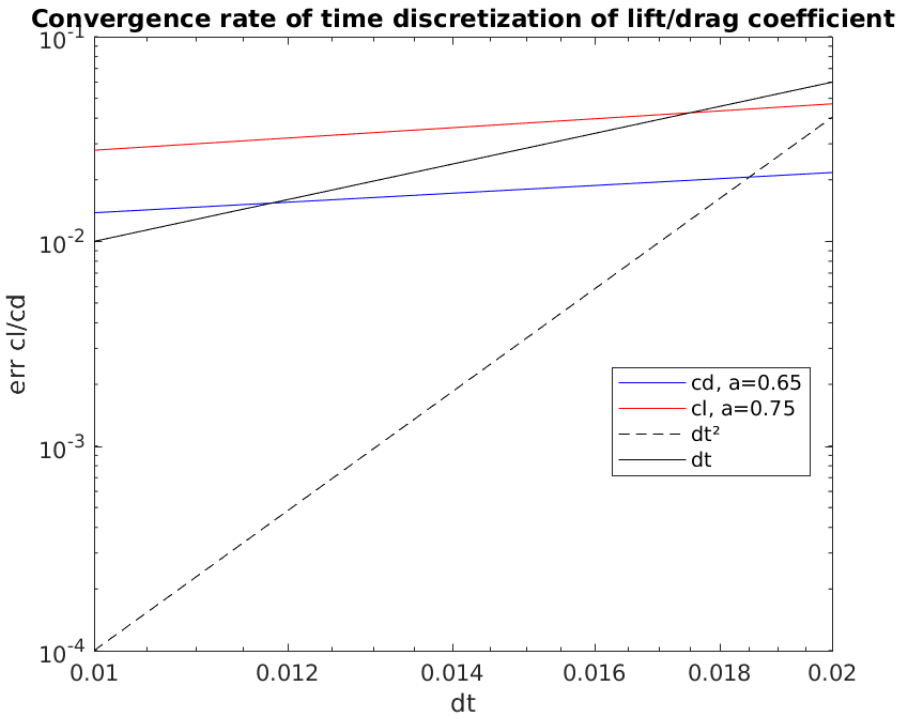

Figure 5.2: Convergence rate of time discretization for time step refinement for flow over a circular cylinder at Re=100, Ma=0.25 with 441x261 grid, $\Delta h = \Delta x = \Delta y = D/50$, $\Delta t = 10^{-2}$

$$r = max_{i,j} \left\{ \frac{\mu_{i,j}}{\rho_{i,j}} \frac{\gamma}{Pr} (\frac{1}{\Delta x^2} + \frac{1}{\Delta y^2}) \Delta t \right\} \tag{5.2}$$

where r is the von Neumann number, μ,ρ,γ,Pr are the viscosity of the fluid, the density of the fluid, the ratio of specific heats $\gamma = c_p/c_v$ and the Prandtl number $Pr = \frac{\mu c_p}{\kappa}$. The stability limit for the von Neumann number is:

$$r \leq \frac{1}{2}$$

The largest von Neumann number was for the moving cylinder simulations where r=0.18 was obtained.

5.2.2 Moving cylinder

It would be interesting to investigate the order of the temporal discretization of the movement of the immersed boundary. However the temporal error of the movement is expected to be strongly coupled to the spatial grid resolution as the spatial error is expected to dominate the total error, unless a extremely fine grid is used. The temporal integration is done

Table 5.2: Table of c_l and c_d convergence values for time step and grid refinement with constant CFL=0.3 for flow over a circular cylinder at Re=100, Ma=0.25 with 441x261 grid, $\Delta h = \Delta x = \Delta y = D/50$, $\Delta t = 10^{-2}$

Grid	$c_{l,\text{peak to peak}}$	$err(c_l)$	$\overline{c}_d$	$err(\overline{c}_d)$
$f(2\Delta h, 2\Delta t)$	0.4411	0.1953	1.1458	0.1253
$f(\Delta h, \Delta t)$	0.5964	0.04	1.2344	0.0367
$f(\frac{\Delta h}{2}, \frac{\Delta t}{2})^*$	0.6364	-	1.2711	-
Tritton [32](exp), Re=97.3,Ma=0	-	-	1.26	-
Canuto and Taira [2], Re=100,Ma=0.25	0.650	-	1.336	-
Karagiozis et al. [10], Re=100,Ma=0.25	0.638	-	1.378	-

* *reference solutions*

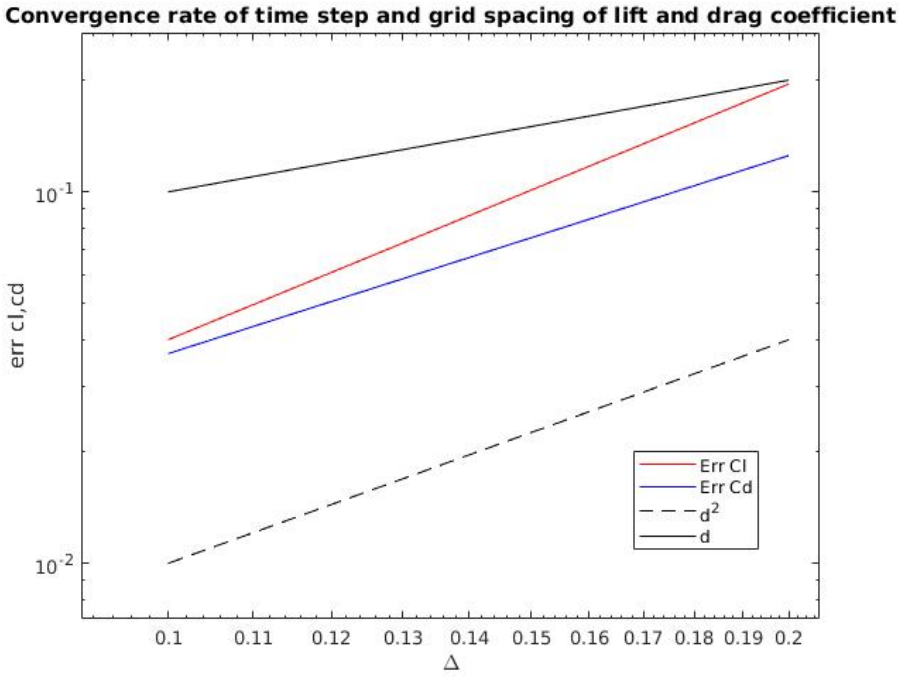

Figure 5.3: Convergence rate of time step and grid space refinement for flow over a circular cylinder at Re=100, Ma=0.25 with 441x261 grid, $\Delta h = \Delta x = \Delta y = D/50$, $\Delta t = 10^{-2}$

by an explicit method, which imposes an upper limit for the CFL-number and the von Neumann number. The CFL- and viscous stability limit restricts the time step size by the grid spacing. The investigation of very large time steps is therefore not possible. An investigation of very small time steps is possible, but the temporal error is expected to be much smaller than the spatial error and so the temporal error will not be visible.

5.3 Validation

The present IBM has been validated by Khalili et al. [11][12] for flow over a stationary circular insulated cylinder in crossflow, flow in quiescent fluid and crossflow for inline- and transversely oscillating cylinder, respectively. In this work simulation of flow over an isothermal stationary cylinder in crossflow in section 5.3.2 and isothermal transversely oscillating cylinder in crossflow in section 5.3.3 is to be validated. The validation of the simulations for an adiabatic cylinder in crossflow is discussed in section 5.3.1.

5.3.1 Adiabatic cylinder in crossflow

The simulations used for verification of the accuracy of the method in section 5.2.1 are discussed. They were ran at Re=100, $Ma_\infty = 0.25$. The results for the lift and drag coefficients are given in table 5.1. A plot of the instantaneous vorticity, ω_z, results for the steady cylinder at non dimensional time t=650 is given in figure 5.4 for the 441x261 grid. The expected von Karman vortex street discussed in section 5.1.1 are visible in this figure. A check of whether the results are reasonable is given in table 5.1 and 5.2, where the lift and drag coefficients are compared to other articles. From the results in table 5.2 the simultaneous grid spacing and time step refinement study indicates that the solution trends towards the results of previous studies numerical studies [10][2] under refinement. The lift coefficient is in good correspondence with these results for the finest solution $f(\frac{\Delta h}{2}, \frac{\Delta t}{2})^*$. The drag coefficient also trends towards the numerical results of [10][2]. The present results of the calculated drag coefficient is closer to the experimental data of [32] than these previous numerical simulations [10][2]. From this convergence study it is not clear that the results have properly converged and further grid spacing refinement should be conducted.

The time step size convergence study presented in table 5.1 yielded results that trended away from the results of [10][2] under time step refinement. This is the opposite of what is expected. These results also trend away from the results of the finest grid and time step solution, $f(\frac{\Delta h}{2}, \frac{\Delta t}{2})^*$. This indicates that the refinement was not carried out correctly. The suspected reason for these results is that the solutions are not fully developed at time, t=650, when the simulations were ended. The lift and drag coefficients should converge towards an oscillating solution. By this line of thought the large time step solutions appear to more quickly develop to the fully developed solution. This should affect the solutions for the simultaneous space and time convergence study as well. The effects of further time development should be inspected by running longer simulations.

A validation study of this method for a corresponding case is also done in [11].

5.3.2 Isothermal cylinder in crossflow

Simulations were done with the isothermal boundary condition described in section 4.7 at $Ma_\infty = 0.01$ and Reynolds numbers Re=40 and Re=20, respectively. These were done as to be comparable with the numerical results of [24], [16] and [1] for validation of the IBM. The imposed wall temperature at the cylinder boundary was $T' = 0.04$ in non-dimensional perturbation form. In figure 5.5 the temperature perturbation, $T' = T - T_0$, for the steady cylinder simulation at Re=20 is shown. The ghost point values inside the cylinder are

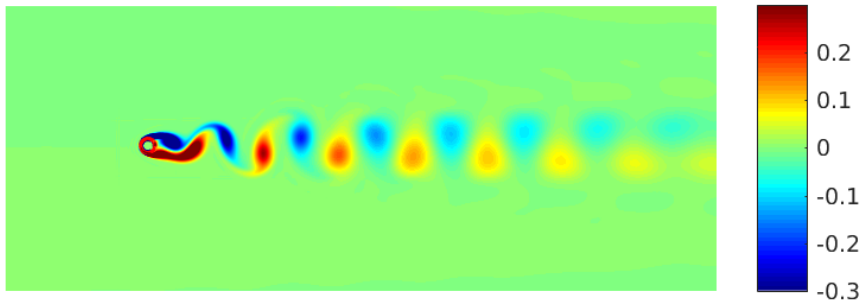

Figure 5.4: Plot of vorticity for steady cylinder, Re=100, Ma=0.25

included to illustrate how the immersed boundary values are enforced. Comparison of the average Nusselt number for different Reynolds numbers is presented in table (5.3). The average Nusselt number for these simulations show good correspondence with other results, both for Reynolds number 40 and 20. The results also coincide quite well with the lift and drag coefficient results for adiabatic cylinders, see table 5.4, of [16][24].It is also here indicated that the drag coefficients achieved by this IBM is usually lower than those calculated by other methods.

The Nusselt number distribution over the cylinder surface for Reynolds number 20 is plotted in 5.6 and compared to the results of Luo et al. [16] and Pan [24]. From this the distribution fits quite well with previous numerical results. However the computed Nusselt number appears to deviate near the front and back of the cylinder, $\theta = 0$ and 180 degrees respectively. This could be owing to the first order approximation used for the Nusselt number calculation.

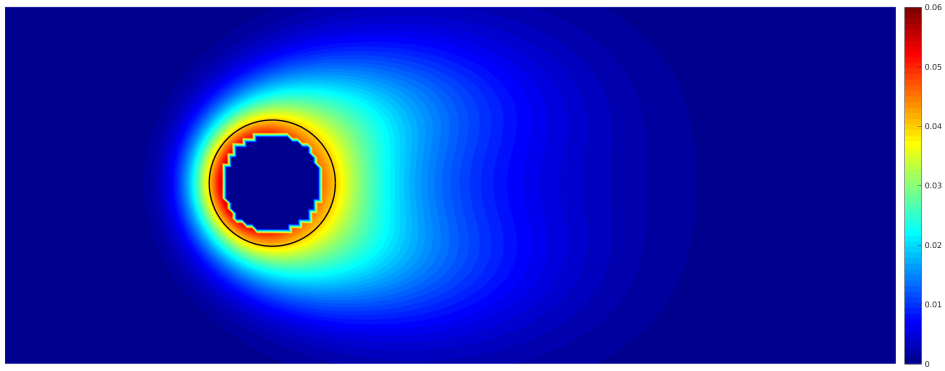

Figure 5.5: Plot of dimensionless temperature perturbation,$T' = T - T_0$, for steady cylinder, Re=20, Ma=0.01

Table 5.3: Calculated average Nusselt number for different studies, Re=40 and 20, Ma=0.01

Comparison of Nusselt numbers			
Study	Re	Pr	$\mathrm{Nu}_{average}$
Present	20	0.7	2.3802
Luo et al. [16]	20	0.7	2.4336
Bharti et al. [1]	20	0.7	2.4653
Pan [24]	20	0.71	2.4553
Present	40	0.7	3.2109
Luo et al. [16]	40	0.7	3.2466
Bharti et al. [1]	40	0.7	3.2825
Pan [24]	40	0.71	3.2563

Table 5.4: Calculated lift and drag coefficients for isothermal cylinder at Re=40 and 20, Ma=0.01

Comparison of drag coefficient c_d		
Study	Re	c_d
Present	20	1.860
Luo et al. [16]	20	2.117
Pan [24]	20	2.039
Tritton [32]	20	2.09
Present	40	1.480
Luo et al. [16]	40	1.578
Pan [24]	40	1.522
Tritton [32](exp)	40	1.58

5.3.3 Isothermal transversely oscillating cylinder in crossflow

Simulations were done with the isothermal boundary condition described in section 4.7 at $Ma_\infty = 0.01$ and Reynolds number Re=200. The oscillation of the cylinder is imposed as described in section 5.1.2. The imposed wall temperature at the cylinder boundary was $T' = 0.2$ in non-dimensional perturbation form. Few experimental results are available for heat transfer for low Reynolds number oscillating cylinders. The results of Cheng and Chen [4] was intended to be used for validation for this case for Re=200. As stated in section 5.1.2 the imposed oscillating cylinder movement did not correspond to the oscillating frequency of the cylinder in [4]. Thus these results are not comparable. The achieved results are presented in table (5.5) and a plot of the calculated perturbation temperature field is presented in figure 5.7. The plot, 5.7, indicates that the oscillating movement has been imposed as the high temperature of the cylinder appears to have been convected in an oscillating manner. The average Nusselt number, presented in table 5.5 does however compare poorly to the results of [4]. As the imposed oscillating movement is at a very low frequency the results should resemble the results for a stationary cylinder to a higher degree. The opposite is observed as the average Nusselt number of this study is higher than

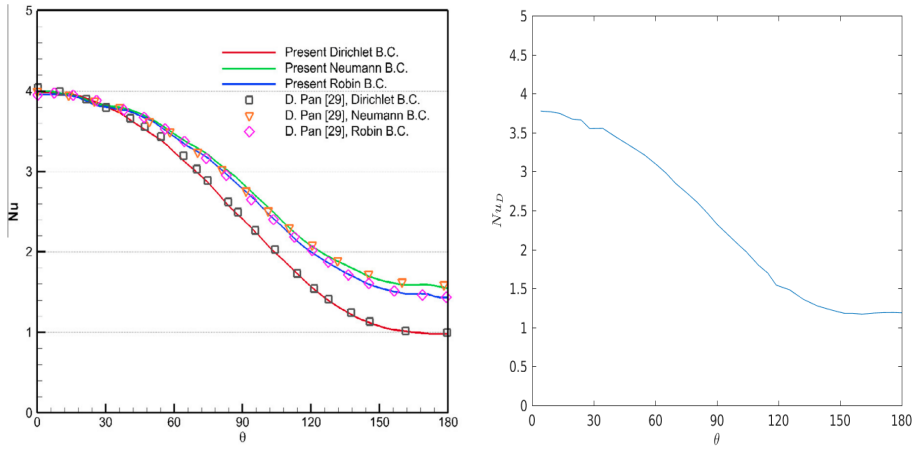

Figure 5.6: Nusselt number distribution over the cylinder surface, Re=20, Ma=0.01
(left) Results of Luo et al. [16] and Pan [24], Dirichlet results correspond to isothermal b.c., *(right)* Present results with 441x261 grid

for both the stationary and oscillating cylinder of [4]. This indicates that the solution is not well enough resolved. The Nusselt number distribution over the cylinder surface is shown in figure (5.8). From this distribution it is evident that the resolution of the temperature gradient near the cylinder is to poor. This could be owing to the first order approximation used or the large time step. The time step for these simulations was $\Delta t = 2 \cdot 10^{-2}$, two times coarser than the time step used in the low Reynolds number simulations.

Table 5.5: Calculated Average Nusselt number for oscillating and stationary cylinder at Re=200

Study	Nu_D
Present, oscillating (A/D=0.628, ω=0.0016)	14.5
Cheng and Chen [4], oscillating (A/D=0.628, ω=0.0016)	8.8
Cheng and Chen [4], stationary	8.0

5.4 Computing time

The computations were done on an ASUS G771J portable computer with Intel i7-4710HQ 4-cores processor with 2.8 GHz frequency. CPU-time for a simulation with 32 000 time steps of size $\Delta t = 2 \cdot 10^{-2}$ on a 441x261 grid was 42309 seconds.

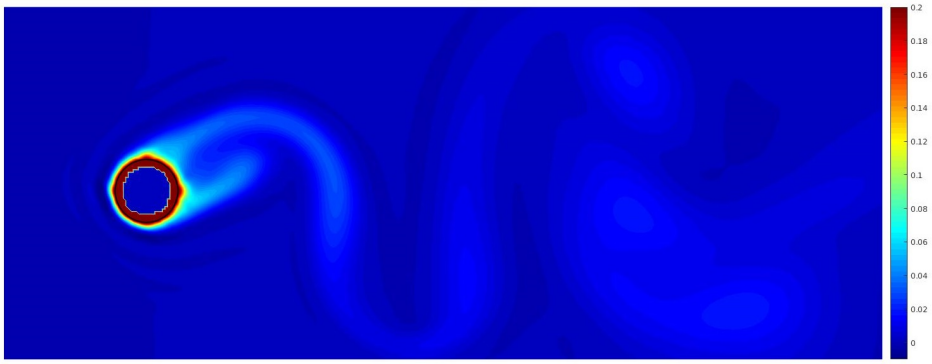

Figure 5.7: Plot of dimensionless temperature perturbation, $T' = T - T_0$, for oscillating cylinder, Re=200, Ma=0.01, A=0.628D, ω=0.0016, dimensionless time t=2000

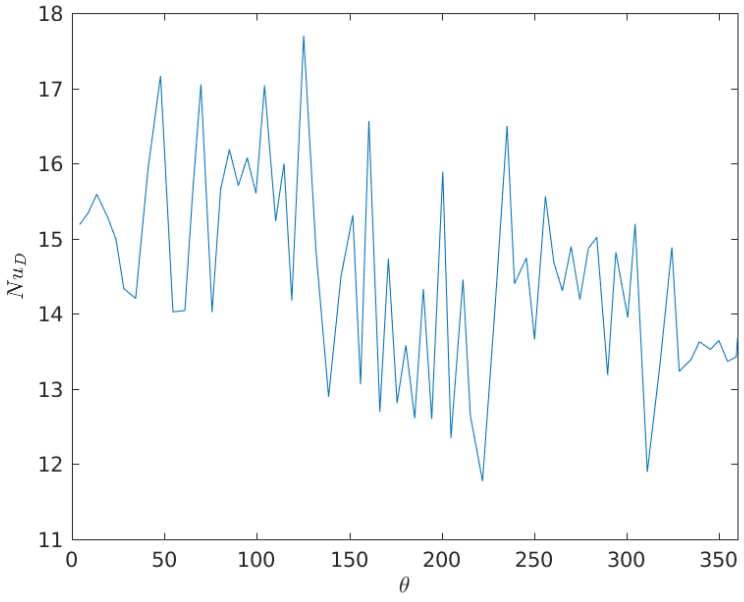

Figure 5.8: Plot Nusselt number distribution for oscillating cylinder, Re=200, Ma=0.01, A=0.628D, ω=0.0016, dimensionless time t=2000

Chapter 6

Conclusions

The purpose of this report is to further verify and validate the higher order ghost-point immersed boundary method by Khalili et al. [11] for moving boundaries. The method has been extended to include isothermal boundary conditions and shows good agreement with experimental and numerical results for stationary cylinders. The convergence of this immersed boundary method has been investigated and shows second order convergence for steady flow over a circular cylinder at Re=100.

Chapter 7

Future outlook

Many aspects of the current work have been left for future work due to computational- and time restrictions. Some suggested points to investigate are listed below:

- The suggested boundary condition (b.c.) improvement for pressure (section 4.7.1) should be further investigated. One interesting aspect to investigate with this BC is how the improvement varies for different Reynolds numbers and grid sizes.
- This b.c. could be expanded to include the variation of viscosity near the wall. This could give an improvement for the very low Reynolds number solutions.
- A proper evaluation and investigation of the temporal order of the moving boundary operation is of interest, this would require a novel approach to the estimation of the temporal error as the temporal error is not visible over the dominating spatial error.
- Investigation of the immersed boundary method for isothermal moving bodies should be furthered as to further validate this IBM.
- The extension of this method into the third dimension is one aspect that would be of interest.
- Implementation of an adaptive mesh refinement (AMR) to improve grid quality in flow regions where high resolution is of importance, such as boundary layers, is an interesting aspect for further study.
- A fluid structure interaction model could be implemented with the immersed boundary method to get an understanding of the interaction between fluid and biomechanical tissue which is part of the goal of the OSAS-research project.

Bibliography

[1] Bharti, R., Chhabra, R., Eswaran, V., May 2007. A numerical study of the steady forced convection heat transfer from an unconfined circular cylinder. Heat and Mass Transfer 43 (7), 639–648.

[2] Canuto, D., Taira, K., December 2015. Two-dimensional compressible viscous flow around a circular cylinder 785, 349–371.

[3] Carpenter, Gottlieb, Abarbanel, 1994. Time-stable boundary conditions for finite-difference schemes solving hyperbolic systems: Methodology and application to high-order compact schemes. Journal of Computational Physics 111 (2).

[4] Cheng, C.-H., Chen, H.-N., 1997. Experimental study of the effect of transverse oscillation on convection heat transfer from a circular cylinder. Journal of Heat Transfer 119 (3), 474–482.

[5] Doost, S. N., Ghista, D., Su, B., Zhong, L., Morsi, Y. S., August 2016. Heart blood flow simulation: a perspective review.(report). BioMedical Engineering OnLine 15 (1).

[6] Fadlun, E., Verzicco, R., Orlandi, P., Mohd-Yusof, J., June 2000. Combined immersed-boundary finite-difference methods for three-dimensional complex flow simulations. Journal of Computational Physics 161 (1), 35–60.

[7] Ghias, R., Mittal, R., Dong, H., 2007. A sharp interface immersed boundary method for compressible viscous flows. Journal of Computational Physics 225 (1), 528–553.

[8] Gustafsson, B., 2008. High Order Difference Methods for Time Dependent PDE. Vol. 38 of Springer Series in Computational Mathematics. Springer Berlin Heidelberg, Berlin, Heidelberg.

[9] Hylla, E., Thiele, F., 2013. Fluid-structure-interaction applying a ghost-cell immersed boundary method. Vol. 121. pp. 473–480.

[10] Karagiozis, K., Kamakoti, R., Pantano, C., 2010. A low numerical dissipation immersed interface method for the compressible navierstokes equations. Journal of Computational Physics 229 (3), 701–727.

[11] Khalili, E., Larsson, M., Müller, B., 2017. Immersed boundary method for the compressible navier-stokes equations uning high order summation by parts difference operators. Progress in Applied CFD CFD2017.

[12] Khalili, E., Larsson, M., Müller, B., 2017. Immersed boundary method for viscous compressible flows around moving bodies. Submitted for publication.

[13] Kim, S. K., Na, Y., Kim, J.-I., Chung, S.-K., 2013. Patient specific cfd models of nasal airflow: Overview of methods and challenges. Journal of Biomechanics 46 (2), 299 – 306, special Issue: Biofluid Mechanics.
URL http://www.sciencedirect.com/science/article/pii/S0021929012006744

[14] Kreiss, H.-O., Scherer, G., 1974. Finite element and finite difference methods for hyperbolic partial differential equations. Mathematical aspects of finite elements in partial differential equations (33), 195–212.

[15] Kreiss, H.-O., Scherer, G., 1977. On the existence of energy estimates for difference approximations for hyperbolic systems. Tech. rep., Dept. of Scientific Computing, Uppsala University.

[16] Luo, K., Zhuang, Z., Fan, J., Haugen, N. E. L., January 2016. A ghost-cell immersed boundary method for simulations of heat transfer in compressible flows under different boundary conditions. International Journal of Heat and Mass Transfer 92, 708–717.

[17] Manish, S., September 2016. A sharp interface immersed boundary method for moving geometries with mass conservation and smooth pressure variation. Computers and Fluids 137, 15–35.

[18] Mattsson, K., Nordström, J., 2004. Summation by parts operators for finite difference approximations of second derivatives. Journal of Computational Physics 199 (2), 503–540.

[19] Mittal, R., Dong, H., Bozkurttas, M., Najjar, F., Vargas, A., Von Loebbecke, A., 2008. A versatile sharp interface immersed boundary method for incompressible flows with complex boundaries. Journal of Computational Physics 227 (10), 4825–4852.

[20] Müller, B., 2008. High order numerical simulation of aeolian tones. Computers and Fluids 37 (4), 450–462.

[21] Nam, J., Lien, F., January 2014. A ghost-cell immersed boundary method for large-eddy simulations of compressible turbulent flows. International Journal of Computational Fluid Dynamics 28 (1-2), 41–55.
URL http://search.proquest.com/docview/1770321784/

[22] Narracott, A. J., Zervides, C., Diaz, V., Rafiroiu, D., Lawford, P. V., Hose, D. R., March 2010. Analysis of a mechanical heart valve prosthesis and a native venous valve: Two distinct applications of fsi to biomedical applications. International Journal for Numerical Methods in Biomedical Engineering 26 (34), 421–434.

[23] Owlcation, C. K., 2017. Non-respiratory Functions of the Respiratory System.
URL https://usercontent2.hubstatic.com/8214455_f1024.jpg

[24] Pan, D., April 2012. A general boundary condition treatment in immersed boundary methods for incompressible Navier-Stokes equations with heat transfer. Numerical Heat Transfer, Part B: Fundamentals 61 (4), 279–297.

[25] Park, H., Gharib, M., February 2001. Experimental study of heat convection from stationary and oscillating circular cylinder in cross flow. Journal of Heat Transfer (Transactions of the ASME) 123 (1), 51–62.
URL http://search.proquest.com/docview/27038027/

[26] Peskin, C. S., 1972. Flow patterns around heart valves: A numerical method. Journal of Computational Physics 10 (2), 252–271.

[27] Poinsot, T.-J., Lele, S., 1992. Boundary conditions for direct simulations of compressible viscous flows. Journal of Computational Physics 101 (1), 104129.

[28] Pottebaum, T. S., Gharib, M., 2006. Using oscillations to enhance heat transfer for a circular cylinder. International Journal of Heat and Mass Transfer 49 (17), 3190–3210.

[29] Schlichting, H., 1979. Boundary-layer theory.

[30] Strand, B., 1994. Summation by parts for finite difference approximations for d/dx. Journal of Computational Physics 110 (1).

[31] Sun, J., Shao-Fan, C., January 2017. The development of a terrain-resolving scheme for the forward model and its adjoint in the four-dimensional variational Doppler radar analysis system (vdras). Monthly Weather Review 145 (1), 289–306.
URL http://search.proquest.com/docview/1924591734/&pq_origsite=primo

[32] Tritton, D. J., November 1959. Experiments on the flow past a circular cylinder at low Reynolds numbers. Journal of Fluid Mechanics 6 (4), 547–567.

[33] Tyagi, M., Roy, S., Harvey III, A. D., Acharya, S., 2007. Simulation of laminar and turbulent impeller stirred tanks using immersed boundary method and large eddy simulation technique in multi-block curvilinear geometries. Chemical Engineering Science 62 (5), 1351–1363.

[34] Wang, L., Wu, C., May 2010. An adaptive version of ghost-cell immersed boundary method for incompressible flows with complex stationary and moving boundaries. Science China Physics, Mechanics and Astronomy 53 (5), 923–932.

[35] Xia, J., Luo, K., Fan, J., August 2014. A ghost-cell based high-order immersed boundary method for inter-phase heat transfer simulation. International Journal of Heat and Mass Transfer 75, 302–312.

[36] Xia, J., Luo, K., Fan, J., October 2015. Simulating heat transfer from moving rigid bodies using high-order ghost-cell based immersed-boundary method. International Journal of Heat and Mass Transfer 89, 856–865.

[37] Zdravkovich, M. M., 2007. Flow Around Circular Cylinders, Vol. 1: Fundamentals. Vol. 4. Oxford University Press.

NTNU – Trondheim
Norwegian University of
Science and Technology